Progress towards an accurate determination of the Boltzmann constant by Doppler spectroscopy

2011 New J. Phys. 13 073028

(http://iopscience.iop.org/1367-2630/13/7/073028)

New Journal of Physics
The open-access journal for physics

Progress towards an accurate determination of the Boltzmann constant by Doppler spectroscopy

C Lemarchand, M Triki, B Darquié, Ch J Bordé, C Chardonnet and C Daussy[1]

Laboratoire de Physique des Lasers, UMR 7538, CNRS, Université Paris 13, 99 avenue, J-B Clément, 93430 Villetaneuse, France
E-mail: christophe.daussy@univ-paris13.fr

New Journal of Physics **13** (2011) 073028 (22pp)
Received 17 December 2010
Published 21 July 2011
Online at http://www.njp.org/
doi:10.1088/1367-2630/13/7/073028

Abstract. In this paper, we present the significant progress made by an experiment dedicated to the determination of the Boltzmann constant, k_B, by accurately measuring the Doppler absorption profile of a line in ammonia gas at thermal equilibrium. This optical method based on the first principles of statistical mechanics is an alternative to the acoustical method, which has led to the unique determination of k_B published by the Committee on Data for Science and Technology with a relative accuracy of 1.7×10^{-6}. We report on the first measurement of the Boltzmann constant carried out by using laser spectroscopy with a statistical uncertainty below 10 p.p.m., more specifically 6.4 p.p.m. This progress results from the improvement in the detection method and in the statistical treatment of the data. In addition, we have recorded the hyperfine structure of the probed ν_2 saQ(6,3) rovibrational line of ammonia by saturation spectroscopy and thus determine very precisely the induced 4.36 (2) p.p.m. broadening of the absorption linewidth. We also show that in our well-chosen experimental conditions, saturation effects have negligible impact on the linewidth. Finally, we suggest directions for future work to achieve an absolute determination of k_B with an accuracy of a few p.p.m.

[1] Author to whom any correspondence should be addressed.

Contents

1. Introduction

The renewed interest in the Boltzmann constant is related to the possible redefinition of the International System of Units (SI) [1–12]. A new definition of the kelvin would fix the value of the Boltzmann constant to a value determined by the Committee on Data for Science and Technology (CODATA). Currently, the value of the Boltzmann constant k_B essentially relies on a single acoustic gas thermometry experiment by Moldover *et al* published in 1988 [13, 14] (to avoid confusion with k generally reserved for the wave vector, we denote the Boltzmann constant by k_B throughout this paper). The current relative uncertainty on k_B is 1.7×10^{-6} [15]. In addition to some projects following Moldover's approach [16–19], an alternative approach based on the virial expansion of the Clausius–Mossotti equation and measurement of the permittivity of helium is very promising [20–25]. Since 2004, we have developed a new approach based on laser spectroscopy in which k_B is determined by a frequency measurement. The principle [26, 27] consists in recording the Doppler profile of a well-isolated absorption line of an atomic or molecular gas in thermal equilibrium in a cell. This profile reflects the Maxwell–Boltzmann distribution of velocities along the laser beam axis. In a first experiment, we have demonstrated the potential of this new approach [28–30], on an ammonia rovibrational line. We were soon followed by at least four other groups who started similar experiments on CO_2, H_2O, acetylene and rubidium [31–35].

In this paper, we present the large thermostat used to control the gas temperature and the new spectrometer developed to record the ν_2 saQ(6,3) rovibrational line of ammonia by both linear and saturated absorption spectroscopy. We report on the first measurement of the Boltzmann constant by laser spectroscopy with a statistical uncertainty below 10 p.p.m. and give a first evaluation of the uncertainty budget, which shows that the effect of the hyperfine structure of the probed line needs to be taken into account.

2. The experimental setup

The principle of the experiment consists in recording the linear absorption of a rovibrational ammonia line in the 10 μm spectral region, the ammonia gas being at thermal equilibrium in a cell. The width of such a line is dominated by the Doppler width due to the molecular velocity distribution along the probe laser beam. A complete analysis of the line shape that can take into account collisional effects (including pressure broadening and the Lamb–Dicke–Mossbauer (LDM) narrowing), hyperfine structure, saturation of the molecular transition, optical depth, etc, leads to the determination of the Doppler width and thus to k_B. The e-fold half-width of the Doppler profile, $\Delta\omega_D$, is given by

$$\frac{\Delta\omega_D}{\omega_0} = \sqrt{\frac{2k_BT}{mc^2}},$$

where ω_0 is the angular frequency of the molecular line, c is the velocity of light, T is the temperature of the gas and m is the molecular mass. Uncertainty on k_B is limited by that on mc^2/h (directly deduced from atom interferometry experiments [36–38]), on atomic mass ratios measured in ion traps [39], on the Planck constant h, on T and on the ratio

$$\frac{\Delta\omega_D}{\omega_0}.$$

The probed line is the ν_2 saQ(6,3) rovibrational line of the ammonia molecule $^{14}NH_3$ at the frequency $\upsilon = 28\,953\,693.9\,(1)$MHz. This molecule was chosen for two main reasons: a strong absorption band in the 8–12 μm spectral region of the ultra-stable spectrometer that we have developed for several years and a well-isolated Doppler line to avoid any overlap with neighboring lines [40]. The experiment requires fine control of (i) the laser intensity sent into the absorption cell, (ii) the laser frequency that is tuned over a large frequency range to record the linear absorption spectrum and (iii) the temperature of the gas that has to be measured during the experiment.

2.1. The spectrometer

The spectrometer (figure 1) is based on a CO_2 laser source that operates in the 8–12 μm range. For this experiment, important issues are frequency stability, frequency tunability and intensity stability of the laser system. The laser frequency stabilization scheme is described in [41]: a sideband generated with a tunable electro-optic modulator (EOM) is stabilized on an OsO_4 saturated absorption line detected on the transmission of a 1.6 m-long Fabry–Perot cavity (FPC). The laser spectral width measured by the beat note between two independent lasers is smaller than 10 Hz and the laser exhibits frequency instability of 0.1 Hz (3×10^{-15}) for a 100 s integration time.

Since its tunability is limited to 100 MHz, our CO_2 laser source is coupled to a second EOM which generates two sidebands, SB− and SB+, of respective frequencies $\nu_{SB+} = \nu_L + \nu_{EOM}$ and $\nu_{SB-} = \nu_L - \nu_{EOM}$ on both sides of the fixed laser frequency, ν_L. The frequency ν_{EOM} is tunable from 8 to 18 GHz. The intensity ratio between these two sidebands and the laser carrier is about 10^{-4}. After the EOM, a grid polarizer attenuates the carrier by a factor 200, but not the sidebands that are cross-polarized.

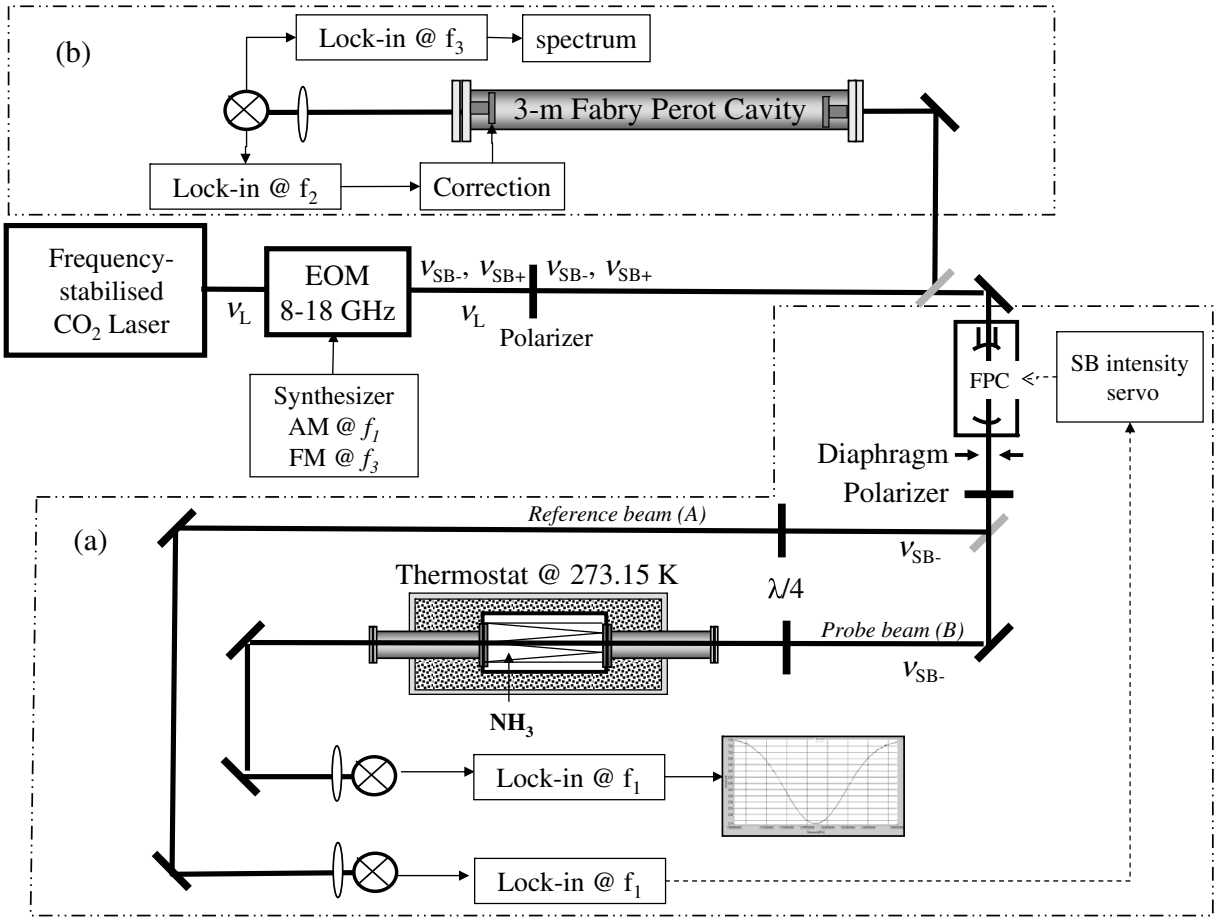

Figure 1. Experimental setup for (a) linear absorption spectroscopy and (b) saturated absorption spectroscopy (AM, amplitude modulation; FM, frequency modulation; EOM, electro-optic modulator; FPC, Fabry–Perot cavity; SB, sideband; lock-in, lock-in amplifier).

Figure 1(b) presents the saturated absorption spectrometer used for recording the hyperfine structure of the rovibrational line, which will be described in section 3. Figure 1(a) represents the linear absorption spectrometer. An FPC with a 1 GHz free spectral range and a finesse of 150 is then used to drastically filter out the residual carrier and the unwanted SB+ sideband and to stabilize the intensity of the transmitted sideband SB−. In order to keep the laser intensity constant at the entrance of the cell during the whole experiment, the transmitted beam is split into two parts with a 50 : 50 beamsplitter: one part feeds a 37 cm-long ammonia absorption cell for spectroscopy (probe beam B), while the other is used as a reference beam (reference beam A). The reference signal A intensity which gives the intensity of the sideband SB− is compared and locked to a very stable voltage reference (stability better than 10 p.p.m.) by acting on the length of the FPC. A suitable intensity discriminator is obtained when the FPC is tuned so that the sideband frequency lies on the slope of the resonance. The absorption length of the cell can be adjusted from 37 cm (in a single-pass configuration) to 3.5 m (in a multi-pass configuration). Both the reference beam (A) and the probe beam (B) which cross the absorption cell are amplitude-modulated at $f_1 = 40$ kHz via the 8–18 GHz EOM for noise

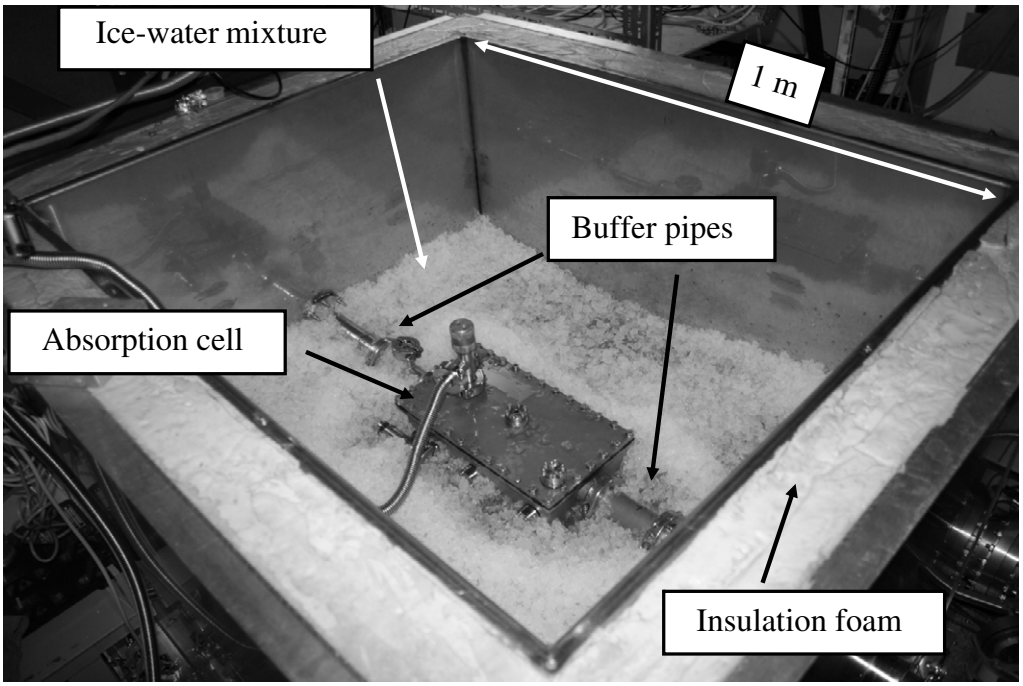

Figure 2. Absorption cell inside the ice–water thermostat.

filtering, and signals are obtained after demodulation at f_1. The probe beam (B) signal then gives the absorption signal of the molecular gas recorded with a constant incident laser power governed by the stabilization of signal A. The sideband is tuned close to the desired molecular resonance and scanned over 250 MHz to record the Doppler profile.

2.2. The thermostat

This experiment requires a thermostat to maintain the spectroscopic cell at a homogeneous temperature [42]. The absorption cell sits in a large thermostat filled with an ice–water mixture in order to set its temperature close to 273.15 K. The thermostat is a large stainless steel box ($1.2 \times 0.8 \times 0.8\,\mathrm{m}^3$) thermally isolated by a 10 cm-thick insulating wall (see figure 2). The absorption cell ($33 \times 18 \times 9\,\mathrm{cm}^3$), placed at the center of the thermostat, is a stainless steel vacuum chamber endowed with two anti-reflective-coated ZnSe windows. From these windows, pumped buffer pipes extend out of the thermostat walls. They are closed on the external side with room temperature ZnSe windows. Vacuum prevents heat conduction and water condensation on windows.

The cell temperature and thermal gradients are measured with long stems 25 Ω standard platinum resistance thermometers (SPRTs) calibrated at the triple point of water and at the gallium melting point. Those SPRTs are compared with a low temperature dependence resistance standard in an accurate resistance measuring bridge. The resulting temperature accuracy measured close to the cell is 1 p.p.m. with a noise of 0.2 p.p.m. after 40 s of integration. For longer integration times, temperature drifts of the cell remain below $0.2\,\mathrm{p.p.m.\,h}^{-1}$. The melting ice temperature homogeneity close to the cell has been investigated. Reproducible residual gradients parallel to the cell walls have been measured: the vertical—respectively horizontal (both directions)—gradient is equal to $0.05\,\mathrm{mK\,cm}^{-1}$,

i.e. 0.17 p.p.m. cm^{-1}—respectively 0.03 mK cm^{-1}, i.e. 0.1 p.p.m. cm^{-1}, leading to an overall temperature inhomogeneity along the cell below 5 p.p.m. These residual temperature gradients probably come from the difficulty of keeping a homogeneous mixture surrounding the cell. Finally, we conclude that the temperature in the experiment is $T = 273.1500\ (7)$ K.

3. Hyperfine structure of the ammonia line

The saQ(6,3) line ($J = 6$ and $K = 3$ are, respectively, the quantum numbers associated with the total orbital angular momentum and its projection on the molecular symmetry axis) has been chosen because it is a well-isolated rovibrational line with long-lived levels (natural width of the order of a few Hz). However, owing to the non-zero spin values of the N and H nuclei, an unresolved hyperfine structure is present in the Doppler profile of the rovibrational line and is responsible for a broadening of the line, which is related to the relative position and strength of the individual hyperfine components. The relative increase of the linewidth due to this hyperfine structure scales as the square of the ratio $\Delta_{\rm hyp}/\Delta\nu_{\rm Dopp}$ (where $\Delta_{\rm hyp}$ is the global spread of the overall hyperfine structure and $\Delta\nu_{\rm D} = \Delta\omega_{\rm D}/2\pi$, the Doppler width), which results in a relatively small influence. In the case of the probed ammonia line, we will see that the hyperfine structure extension of the stronger components is of the order of 50 kHz. However, weaker lines around ±600 kHz away from the main structure must be considered, as they actually give the largest contribution. For a Doppler width of about 50 MHz, the impact may be a few p.p.m. For this reason, it is necessary to have good knowledge of that structure in order to take it into account in the line shape analysis.

3.1. Description of the hyperfine interactions

The hyperfine Hamiltonian of ammonia is very well known [43–45]. The hyperfine structure of the saQ(6,3) line is in part due to the interaction between the nitrogen nuclear quadrupole moment and the gradient of the electric field at the nucleus. Spin–rotation terms come from the interaction between the magnetic field induced by the molecular rotation and the magnetic moment of the nitrogen nucleus and the hydrogen nuclei. The other magnetic hyperfine terms are the spin–spin interactions between N and H atoms or between H atoms themselves. The strength of these interactions is characterized by coupling constants, usually denoted by eQq (N quadrupole constant), R (N spin–rotation constant), S (H spin–rotation constant), T (N–H spin–spin constant) and U (H–H spin–spin constant) according to notations first introduced by Kukolich and Wofsy [46]. Those constants are experimentally accessible. There are two sets of such constants for the fundamental and the upper rovibrational levels. Since the nitrogen nuclear spin is $I_{\rm N} = 1$, each rovibrational level is split into three sub-levels $F_1 = (7, 6, 5)$, where F_1 is the modulus of the sum of the orbital angular momentum and the spin of the nitrogen nucleus, $\vec{F}_1 = \vec{J} + \vec{I}_{\rm N}$. Then, each of these sub-levels is again split into four sub-levels characterized by (F_1, F), where $F = (F_1 \pm 1/2, F_1 \pm 3/2)$ is the modulus of the total angular momentum of the molecule and $\vec{F} = \vec{F}_1 + \vec{I}$. $\vec{I}$ is the total spin of the hydrogen nuclei. Its modulus is equal to 3/2 when K is a multiple of 3 [43].

3.2. Saturation spectroscopy

The first hyperfine structures of ammonia were recorded on a molecular beam in the microwave region [45–47] and led to very good knowledge about the hyperfine constants in the ground

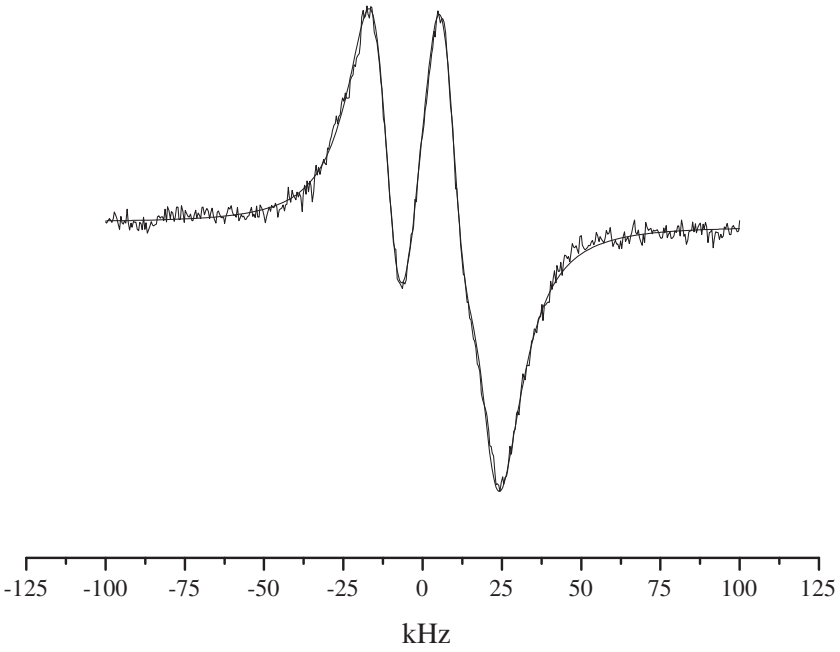

Figure 3. The main $\Delta F_1 = 0$ components of the ν_2 saQ(6,3) experimental spectrum (first harmonic detection) of $^{14}NH_3$ fitted by three derivatives of a Lorentzian.

vibrational level. Saturation spectroscopy of ammonia in the infrared leads to additional information on the upper vibrational level and was first performed by our group, exhibiting both the electric and magnetic hyperfine structure of ammonia [48–50], especially the six components of the asQ(8,7) line, fully resolved in a large 18 m-long absorption cell [51]. From these measurements, the variation of the quadrupole constant and spin–rotation constants with vibration could be obtained. In the present study, a new experimental setup was developed to record the hyperfine structure of the saQ(6,3) rovibrational line by saturated absorption spectroscopy (see figure 1(b)). A 3 m-long FPC in a plano-convex configuration with a convex mirror radius of 100 m and a finesse of about 140 is filled with ammonia. The red detuned SB− sideband generated by the 8–18 GHz EOM feeds this FPC. Two frequency modulations, f_2 and f_3, are required for this experiment. The modulation f_2 is used to stabilize the resonator frequency and can be applied either on one mirror mounted on a piezoelectric transducer or directly on the sideband frequency via the synthesizer that drives the 8–18 GHz EOM. The hyperfine components of the molecular line are detected in the transmission of the cavity after demodulation at f_3, a modulation applied on the sideband frequency via the EOM. Experimental parameters were first optimized to reduce as much as possible the linewidth in order to clearly observe the three main $\Delta F_1 = 0$ lines. On the spectrum displayed in figure 3, those main components are well fitted by first derivatives of Lorentzians. Each line presents an unresolved structure of four $\Delta F = 0$ components. The modulation applied on the FPC for its frequency stabilization was at 11 kHz and the sideband modulation frequency for the molecular lines detection was equal to 1 kHz with a depth of 2 kHz. The resolution was limited by laser intensity (around 1 mW inside the FPC), gas pressure (10^{-5} mbar), modulation settings and transit time broadening. The absorption signal was recorded over 200 kHz with 500 points and 30 ms integration time per point.

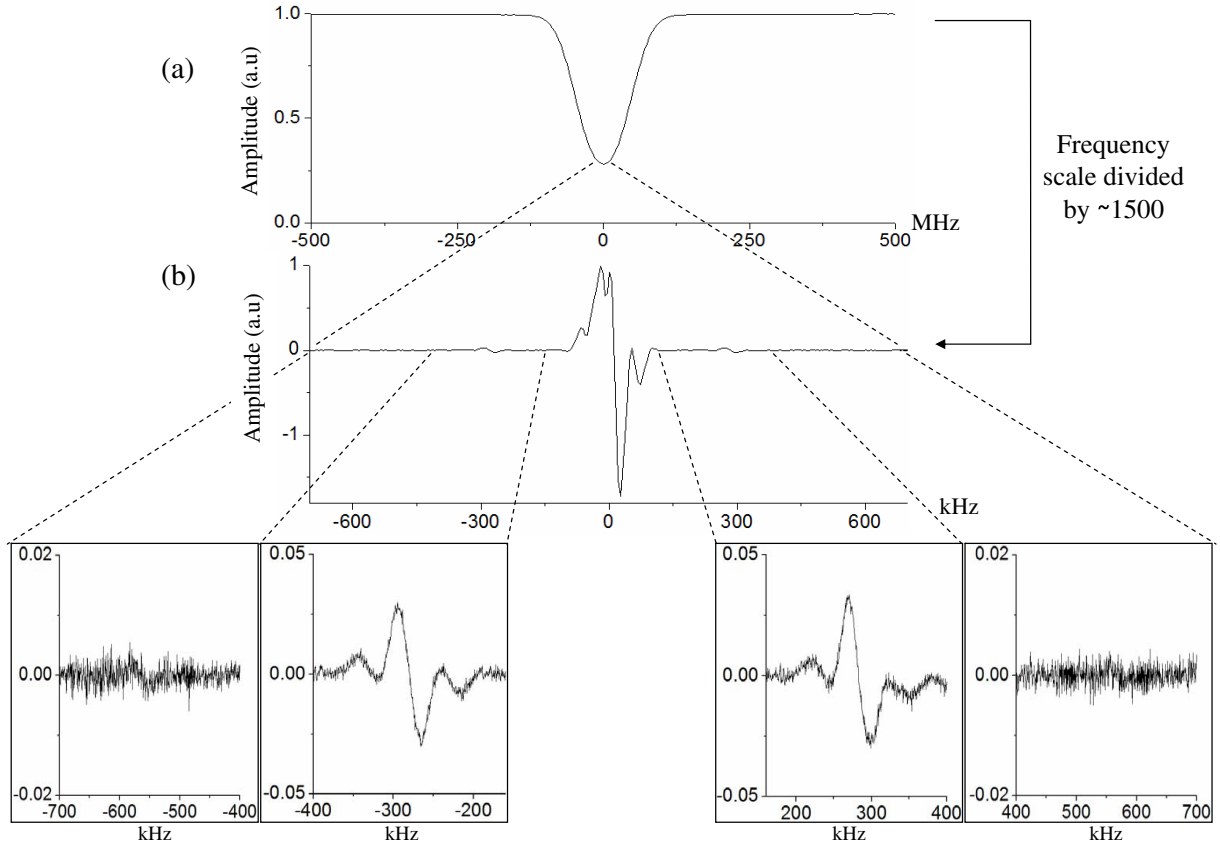

Figure 4. $^{14}NH_3$ saQ(6,3) absorption line recorded by linear absorption (a) and at higher resolution by saturated absorption spectroscopy (b). At about 300 kHz on both sides of the central components, Doppler-generated level crossings (between $\Delta F = 0$ and $\Delta F = \pm 1$) are observed. At about 600 kHz from the central resonances satellite, weaker components are expected.

The experimental hyperfine spectrum of figure 3 has been fitted with three derivatives of a Lorentzian line shape. The adjustable parameters were the baseline offset and slope, the line central frequency, the intensity scale, the full-width at half-maximum of the Lorentzian (identical for the three components), ΔeQq and ΔR, respectively, the change in the quadrupole coupling constant and in the N spin–rotation constant between the upper and lower levels. Figure 3 illustrates excellent agreement between experimental data and the numerical adjustment.

These 12 partially resolved lines are the strongest lines corresponding to an approximate selection rule $\Delta J = \Delta F_1 = \Delta F$. In fact, 66 weaker transitions are also allowed and will contribute to the Doppler signal and broaden it. Doppler-generated level crossing resonances can also be observed in saturated absorption (but are not present in linear absorption spectroscopy) and give signal at the mean frequency between the two involved transitions. Figure 4 compares (a) the ν_2 saQ(6,3) linear absorption signal (recorded over 1 GHz using sideband amplitude modulation at $f_1 = 40$ kHz and first harmonic detection; see section 2.1) and (b) the saturated absorption signal recorded over 1.4 MHz in the transmission of the 3 m-long FPC. In the latter case, experimental parameters have been adjusted to optimize the signal-to-noise ratio in order

to be able to observe the expected weak satellite transitions. The cost to be paid is a degradation of the resolution and a slight distortion of the line shape. All frequency modulations were directly applied on the sideband. A 90 kHz frequency modulation (60 kHz depth) was used for the resonator frequency stabilization. For molecular line detection a 10 kHz frequency modulation (30 kHz depth) was applied and first harmonic detection was used (with 30 ms integration time per point).

Under these experimental conditions, the three intense $\Delta F_1 = 0$ multiplets are strongly broadened by the frequency modulation. Signal of Doppler-generated level crossings (between $\Delta F = 0$ and $\Delta F = \pm 1$) is clearly observed around ± 300 kHz from the central components. For a frequency detuning of about ± 600 kHz from the central components, signals coming from very weak $\Delta F = \pm 1$ satellite components and crossovers between $\Delta F = +1$ and $\Delta F = -1$ are hardly distinguishable.

3.3. Analysis of the hyperfine structure

Clearly, the recorded spectra do not allow the determination of the whole set of hyperfine constants. In particular, we can only measure the position of the center of gravity of each series of crossover resonances. However, the numerous studies of hyperfine structures in the ground vibrational level [45–47] allow us to accurately fix the value of the hyperfine constants at the $\nu_2 = 0$ level:

$$eQq_0 = -4018(1)\,\text{kHz}, \quad R_0 = 6.75(1)\,\text{kHz}, \quad S_0 = -18.00(1)\,\text{kHz}, \quad T_0 = -0.85(1)\,\text{kHz}$$
$$\text{and} \quad U_0 = -2.5(3)\,\text{Hz}.$$

Only rovibrational saturation spectroscopy provides information on the hyperfine constants in the $\nu_2 = 1$ level. Our group has recorded in the past the asR(5,0) and asQ(8,7) lines of $^{14}NH_3$ and also the asR(2,0) line of $^{15}NH_3$ [48–51]. These studies give the right order of magnitude of the hyperfine constants in the upper level of the saQ(6,3) transition. The fit of the three main multiplets (figure 3) revealed that the uncertainty on their relative positions was 40 Hz and that this structure was only sensitive to the change in eQq and R between the lower and upper levels, leading to

$$\Delta eQq = eQq_1 - eQq_0 = -196.8(6)\,\text{kHz} \quad \text{and} \quad \Delta R = R_1 - R_0 = -535\,(6)\,\text{Hz}.$$

The other upper state constants were fixed with a conservative uncertainty of 10% to values estimated from our previous studies on the asR(5,0), asQ(8,7) and asR(2,0) lines: $S_1 = -17.5\,(18)$ kHz; $T_1 = -0.9\,(1)$ kHz and $U_1 = -2.5(3)$ Hz.

In principle, the position of the center of gravity of the crossover resonances (with respect to that of the main lines) could give information on the hyperfine structure in both the lower and upper vibrational levels. However, our experimental results, with an accuracy of 400 Hz on that position, although in good agreement with the ground vibrational level hyperfine constants, do not bring enough new information.

Figure 5 shows the hyperfine lines as sticks with relative intensities corresponding to the weak field regime. Apart from the strong main lines, the structure reveals manifolds around ± 600 kHz (see figure 4) and ± 150 kHz (not investigated by saturated absorption spectroscopy).

Using the SPCAT program (developed by H Pickett, Jet Propulsion Laboratory [52]), as well as a homemade saturation spectroscopy simulation program, we checked very carefully

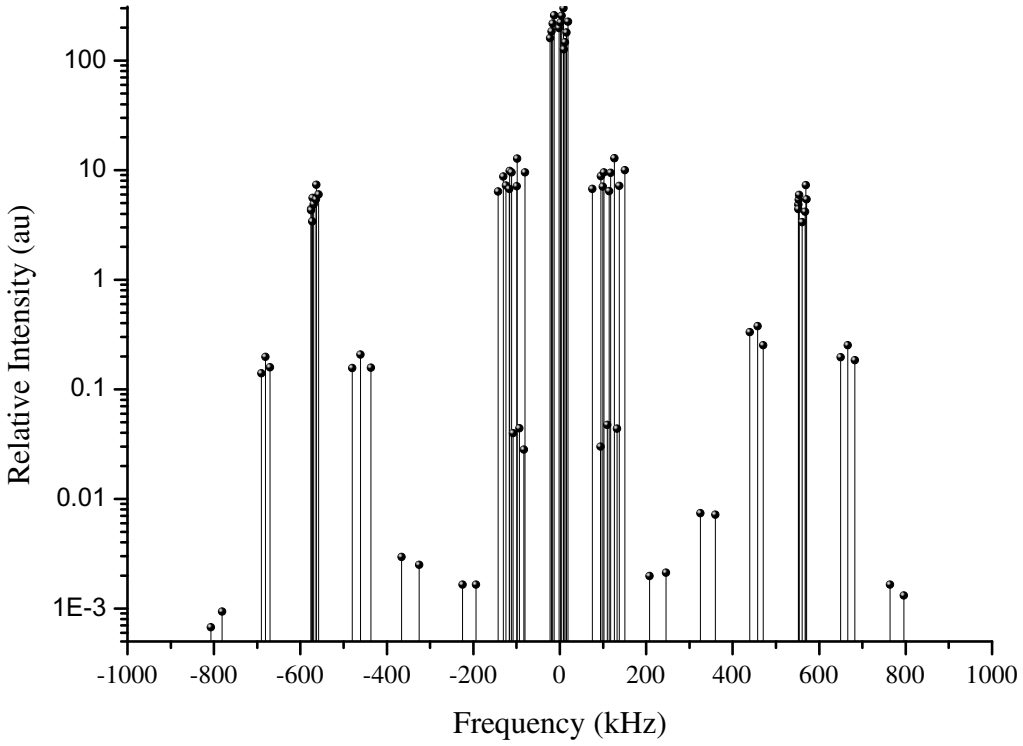

Figure 5. Stick spectrum of the 78 hyperfine components present in the Doppler profile. The height of each stick reflects the intensity (in logarithmic scale) of the corresponding hyperfine transition in linear absorption.

how the positions of the lines and their intensities in linear absorption are affected by a change in the hyperfine constants. This showed that the present knowledge of the hyperfine constants gives a very strong constraint on the hyperfine structure in the Doppler profile of the saQ(6,3), both frequency- and intensity-wise.

As a result of the uncertainty on the values of the hyperfine constants, an uncertainty of 275 Hz on the center of gravity of the crossovers situated around ±300 kHz is deduced. The corresponding uncertainty on the intensities in linear absorption stays below 0.15%. These two effects will fix the uncertainty on the correction due to the hyperfine structure to be applied for the determination of the Doppler width and thus k_B.

4. The Boltzmann constant measurement

4.1. Doppler broadening measurement

4.1.1. Absorption line shape. We consider the case of an optically thick medium under low saturation for which the absorption coefficient for the laser power given by

$$\kappa(\omega) = -\frac{1}{P(z,\omega)}\frac{\mathrm{d}P(z,\omega)}{\mathrm{d}z} \tag{1}$$

leads to the Lambert–Beer law $P(L,\omega) = P(0)\mathrm{e}^{-\kappa(\omega)L}$ (for a total absorption length L) in the linear regime. At low pressure, the absorption coefficient $\kappa(\omega)$ can be described by a Voigt

profile that is the convolution of a Gaussian shape related to the inhomogeneous Doppler broadening and of a Lorentzian shape whose half-width, γ_{ab}, is the sum of all homogeneous broadening contributions. Since the natural width is negligible for rovibrational levels, this homogeneous width is dominated by molecular collisions and is therefore proportional to pressure. In linear absorption spectroscopy and for an isotropic distribution of molecular velocities, it has been recently demonstrated that all transit effects are already included in the inhomogeneous Doppler broadening and do not depend on the laser beam profile, a result that is not intuitive [53]. At high pressure, the LDM effect that results in a reduction of the Doppler width with pressure must be taken into account [54–58]. The absorption coefficient is the Fourier transform of the correlation function of the optical dipole, denoted by $\phi(\tau)$. For the dimensionless absorbance $A(\omega-\omega_{ab}) = \kappa(\omega-\omega_{ab})L$, one finds that [53]

$$A(\omega-\omega_{ab}) = \frac{4\pi\alpha N d_{ab}^2 \omega L e^{(-E_a/k_B T)}}{Z_{int}} \mathrm{Re} \int_0^{+\infty} \exp(-i\omega\tau)\phi(\tau)\,d\tau, \tag{2}$$

where ω is the laser angular frequency, $\omega_{ab} = (E_b - E_a)/h$ the angular frequency of the molecular line (E_a and E_b are the energies of the lower and upper rovibrational levels a and b in interaction with the laser electromagnetic field, $E_a < E_b$), $\alpha = e^2/(4\pi\varepsilon_0\hbar c)$ the fine structure constant (e is the electron charge), N the density of molecules, $d_{ab} = \mu_{ab}/e$ (μ_{ab} is the transition moment) and Z_{int} the internal partition function.

Various theoretical models are available in the literature to describe the correlation function of the optical dipole, depending on the assumption made about the type of collisions between molecules [53, 59]. Among them the Galatry profile [55] makes the assumption of so-called 'soft' collisions between molecules with the introduction of the diffusion coefficient D. The Galatry optical dipole correlation function is then

$$\phi_G(\tau) = \exp\left[i\omega_{ab}\tau - \gamma_{ab}\tau + \frac{1}{2}\left(\frac{\Delta\omega_D}{\beta_d}\right)^2 \{1 - \beta_d\tau - \exp(-\beta_d\tau)\} \right], \tag{3}$$

where $\Delta\omega_D$ is the half-width of the Doppler profile and $\beta_d = k_B T/mD$ the coefficient of dynamical friction (m is the molecular mass). The Galatry absorbance can then be written using the ${}_1F_1$ Kummer confluent hypergeometric function

$$A_G(\omega-\omega_{ab}) = \frac{4\pi\alpha N d_{ab}^2 \omega L e^{(-E_a/k_B T)}}{\Delta\omega_D Z_{int}} \mathrm{Re} \frac{1}{y(\xi)} {}_1F_1\left[1, 1 + \frac{y(\xi)}{\theta}; \frac{1}{2\theta^2}\right], \tag{4}$$

where

$$\theta = \frac{\beta_d}{\Delta\omega_D}, \quad y(\xi) = \frac{1}{2\theta} + \eta - i\xi, \quad \zeta = \xi + i\eta = \frac{(\omega-\omega_{ab}) + i\gamma_{ab}}{\Delta\omega_D}$$

The Galatry profile evolves from a Lorentzian shape in the high-pressure limit to a Voigt profile at low pressure.

At low pressures (small β_d), we can use for the absorbance the first-order expansion in θ:

$$A(\omega-\omega_{ab}) = \frac{4\alpha N d_{ab}^2 \omega L e^{(-E_a/k_B T)}}{\sqrt{\pi}\Delta\omega_D Z_{int}} \left(\mathrm{Re}\, w(\zeta) + \frac{\theta}{12} \mathrm{Re}\, w_1(\zeta) \right), \tag{5}$$

where $w(\zeta)$ and $w_1(\zeta)$ can be expressed in terms of the error function $w(\zeta) = e^{-\zeta^2}\mathrm{erfc}(-i\zeta)$ and

$$w_1(\zeta) = \frac{8}{\sqrt{\pi}}(1-\zeta^2) + 4i\zeta(3-\zeta^2)\exp(-\zeta^2)\mathrm{erfc}(-i\zeta).$$

The absorbance presents two terms: the first one with $w(\zeta)$ corresponds to the Voigt profile when θ, i.e. β_d, tends to zero and the second one with $w_1(\zeta)$ is the LDM correction at first order. The expression (5) turns out to be a very good approximation of the true Galatry profile under our conditions (see below) and has been chosen in the fitting procedure as the reference line shape with the advantage of a much faster computing time.

4.1.2. Measurement and data processing. The absorption profile, whose Doppler width $\Delta\nu_D = \Delta\omega_D/2\pi$ (the main contribution to the width in our experimental conditions) is of the order of 50 MHz, has been recorded over 250 MHz by steps of 500 kHz with a 30 ms time constant. The time needed to record a single spectrum is about 42 s. For 100% absorption, the signal-to-noise ratios is typically 10^3. Since the signal-to-noise ratio was not high enough to leave the parameter β_d as an adjustable parameter, it was kept proportional to the pressure during the numerical adjustment procedure with a proportionality factor deduced from the literature. Following the original Galatry theory (based on S Chandrasekhar's Brownian motion theory), we used the standard diffusion coefficient, found to be equal to $D^0_{NH_3} = 0.15\,\mathrm{cm^2\,s^{-1}}$ at $P_0 = 1$ atm, as measured in [60] in a classical transport study. Spectroscopic measurements of this coefficient have been carried out for other lines of ammonia by A S Pine and co-workers [61], leading to an effective value 20% smaller than a direct measurement by diffusion in the case of the ν_1 band of NH_3. We actually checked that the results of the fits did not change significantly with such a 20% variation of β_d. Note that the LDM effect scales as the ratio of the wavelength to the mean free path. The mean free path between collisions, inversely proportional to the pressure, is related to the diffusion coefficient $l_m = \sqrt{3m/k_BT} \times D^0_{NH_3} \times (P_0/P)$. It is then easy to show that

$$\theta = \sqrt{\frac{3}{8\pi^2}}\frac{\lambda}{l_m}$$

where $\frac{\theta}{12}$ appears as a scaling factor of the LDM term in expression (5). In our pressure conditions (from 2.5 down to 0.1 Pa) this scaling factor varies from 6×10^{-5} to 2×10^{-6}.

Even with β_d kept constant in the fitting procedure, the signal-to-noise ratios of individual spectra were not high enough to disentangle easily the homogeneous and the Doppler width when using usual fitting algorithms. If we rewrite γ_{ab} as gP, where P is the pressure, proportional to the amplitude of absorption, g is a collisional parameter, a parameter shared by all spectra whatever the pressure is. Thus, to make the fitting algorithm converge, we decided to adjust g in such a way that it is constrained to a constant value for all the measured spectra. We first guess an initial realistic value. We fit all the experimental spectra with a Galatry profile, constraining g to its guessed value, leaving only $\Delta\nu_D = \frac{\Delta\omega_D}{2\pi}$, P (both in the amplitude and γ_{ab}), ν_{ab} and the baseline as adjustable parameters. We expect $\Delta\nu_D$ to remain constant when the pressure is varied, if g is chosen to be equal to the correct value. We then plot $\Delta\nu_D$ as a function of P and record the slope s given by a linear regression of these data. We repeat this procedure for different values of g leading to both negative and positive slopes and compute its estimated final value for which

$\Delta\nu_D$ remains constant (within the noise) when the pressure varies. The experimental data are finally fitted again constraining g to this final value. A weighted average of all the $\Delta\nu_D$ gives the best estimate of the Doppler width from which we deduce the Boltzmann constant (see [62] for details of the fitting procedure).

4.2. Statistical uncertainty analysis

4.2.1. First series of experiments. After 16 h of accumulation, 1420 spectra recorded at various pressures (from 0.1 to 1.3 Pa) yielded a statistical uncertainty on k_B of 37 p.p.m., limited by noise detection. The statistical uncertainty was calculated as the weighted standard deviation deduced from the dispersion of the 1420 Doppler linewidth measurements [42, 62]. Weights were obtained as the inverse of the square of error bars deduced from the adjustment of each spectrum. Note that those error bars are about five times smaller than the standard deviation estimated from the total dispersion of the 1420 measurements. We also estimated the error bar on the Doppler width of each spectrum from a computer-based bootstrap method [63]. The error bar obtained by this method is compatible within ±5% with the error bar obtained from the fitting procedure. The discrepancy observed between the Doppler width standard deviation estimated from the dispersion of the 1420 spectra and the error bar of single Doppler width measurements confirmed by these methods has been attributed to slow drifts of the optical alignment of the laser beam in the absorption cell. Indeed the CO_2 laser-based spectrometer and the thermostated cell were located at two separate breadboards. Long-term drifts of the optical alignment induce slow variations of the amplitude of residual interference fringes on the optical path, which are the main source of the baseline instability. This low-frequency effect is not observable on each individual spectrum, but could affect the global dispersion of repeated measurements over a few hours.

4.2.2. New optical arrangement. To overcome this long-term instability, the thermostat and the spectrometer have been placed on a single optical table. Better optical alignment stability combined with improvement in the optical isolation and spatial filtering of the laser beam led to an efficient reduction and control over several days of the residual interference fringes. To reduce statistical uncertainty, we also chose to increase the molecular absorbance $\kappa(\omega - \omega_{ab})L$ by recording spectra at higher pressures. A second series of 7171 spectra has been recorded and fitted for pressures up to 2.5 Pa. A typical absorption line fitted with the exponential of a Galatry profile and normalized residuals are reported in figure 6.

In addition, to better take into account the characteristics of the spectra, the weight of each individual point is attributed by considering the local noise of the spectrum—this is directly related to the intensity noise on the photodetector, which decreases strongly as the absorption changes from 0 to about 100%. The values of the Doppler width of the 7171 spectra recorded over 70 h are displayed in figure 7 and led to a mean Doppler half-width of $\Delta\nu_D = 49.88590(16)$ MHz (3.2 ppm), leading to a statistical uncertainty on the Boltzmann constant determination of 6.4 p.p.m. (figures 8 and 9).

Note that there is still a discrepancy between the Doppler width uncertainty estimated from measurement dispersion and the error bar on each point estimated either from a nonlinear regression or from the bootstrap method, but thanks to the improved long-term stability of the optical alignment, this discrepancy has been reduced by a factor of 2. The 6.4 p.p.m. error bar reflects dispersion of measurements, which includes *de facto* the statistical uncertainty of

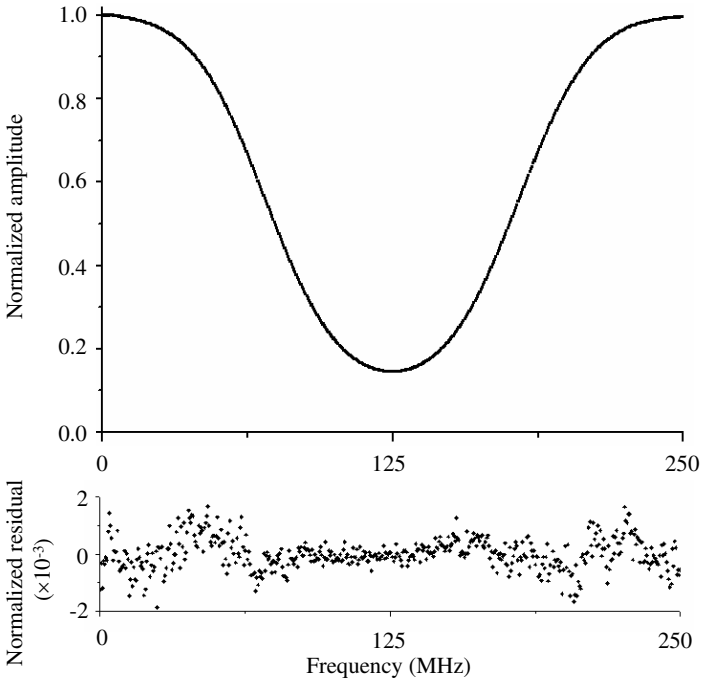

Figure 6. Absorption spectrum recorded at 1.3 Pa and normalized residuals of a nonlinear least-squares fit with the exponential of a Galatry profile Taylor expansion to first order in β_d.

individual measurements and instabilities of the experiment. Two analyses have been performed to validate this statistical limitation. We randomly divided our data set into four equal subsets of points (each randomly ordered) and analyzed those sets independently to obtain four independent mean values of the Doppler e-fold half-width. The dispersion of these four values reported in figure 8 is consistent with the statistical uncertainty of each data subset (twice as high as the 3.2 p.p.m. obtained for 7171 spectra).

In a second analysis, measurements of k_B have been randomly ordered and the relative uncertainty has been calculated as a function of τ, where τ is the accumulated time of measurement (figure 9). The slope of both the red and black curves is proportional to one over the square root of τ. This slope is a good indication of a statistical limitation. The significant improvement in the standard deviation at fixed accumulation time is the conjunction of the better optical stability of the setup, the larger pressure range and the new statistical analysis that also clearly stabilizes the fitting procedure and reduces the dispersion of the data.

4.3. Systematic uncertainty analysis

The k_B measurement may be affected by several systematic effects. In this section, we have listed and investigated some of them: the hyperfine structure of the saQ(6,3) absorption line, the collisional effects, the modulation, the size or shape of the laser beam, the temperature control of the absorption cell, the nonlinearity in the photodetector response and the saturation of the rovibrational transition.

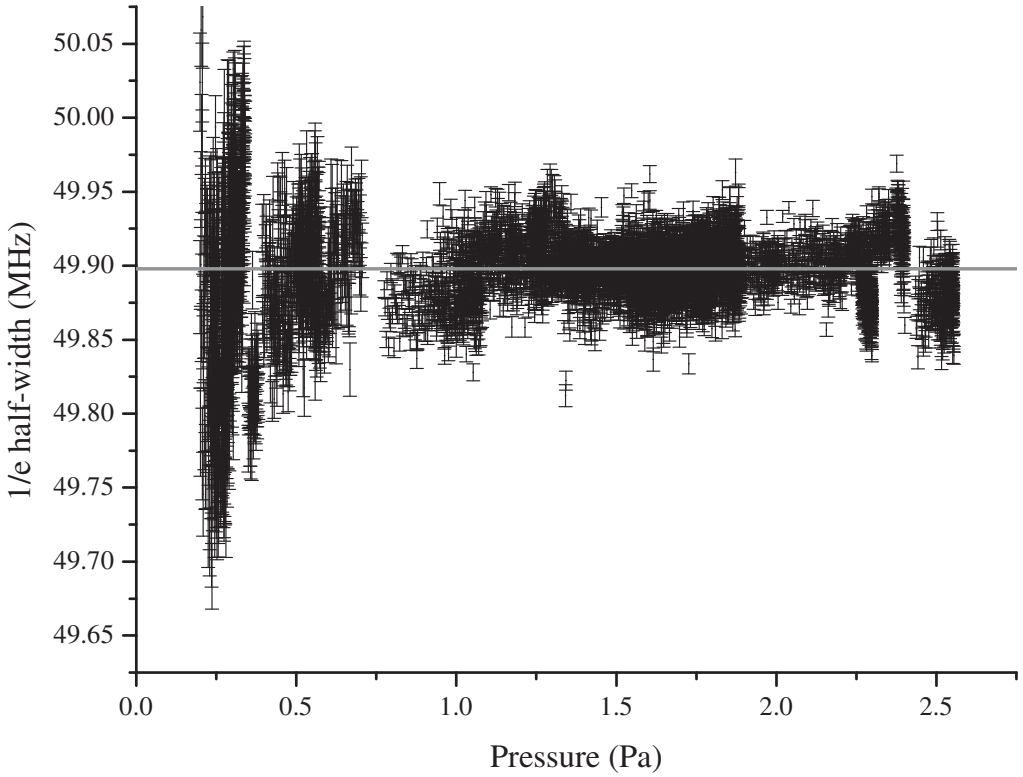

Figure 7. Doppler e-fold half-width of the saQ(6,3) NH_3 absorption line versus pressure, after fitting 7171 spectra with a Galatry profile Taylor expansion to first order in β_d.

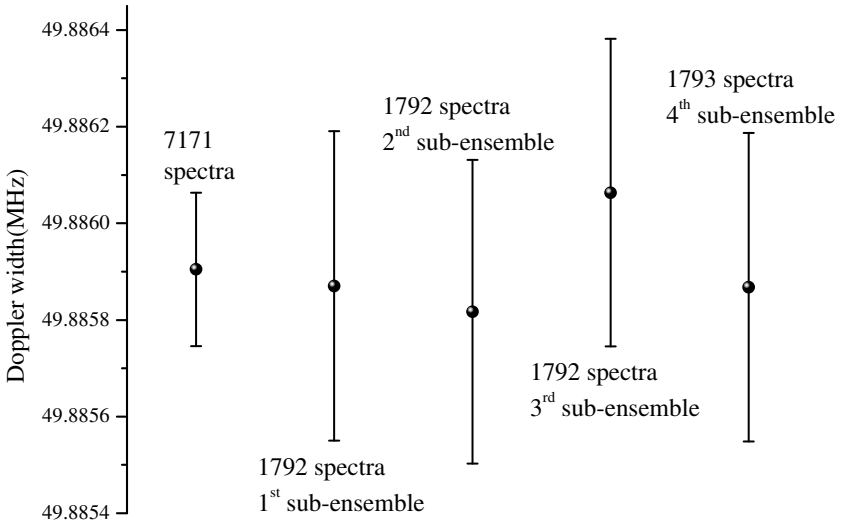

Figure 8. Mean Doppler e-fold half-width and associated uncertainties for the 7171 spectra and for four subsets of these data (three sets of 1792 points and one set of 1793 points) each randomly ordered.

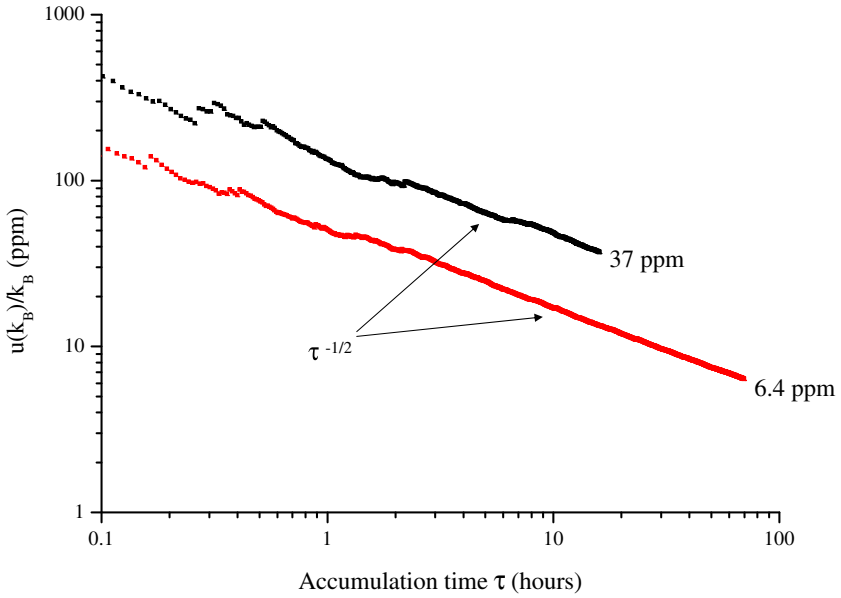

Figure 9. Relative statistical uncertainty $u(k_B)/k_B$ of the Boltzmann constant measurement versus time for 1420 spectra recorded over 16 h and 7171 spectra recorded over 70 h, leading to statistical uncertainties of 37 and 6.4 p.p.m., respectively.

4.3.1. The hyperfine structure. Saturated absorption spectroscopy along with microwave spectroscopy has provided an accurate determination of spectroscopic parameters of the ν_2 saQ(6,3) line (see section 3). The impact of this hyperfine structure on the Doppler width measurement could finally be estimated. The method is straightforward: we sum the Voigt profiles (or Galatry profiles) associated with the 78 hyperfine components of the linear spectrum with positions and intensities precisely determined by the analysis presented in section 3. The resulting line shape is then fitted by a unique Voigt (or Galatry) profile and the difference with the 'true' Doppler width is thus deduced. The 1.1 kHz uncertainty on the global spread of the overall hyperfine structure (twice that on the crossover positions) and the 0.15% uncertainty on the intensities result in a very precise determination of the correction to be applied on the value of k_B: $\left.\frac{\Delta k_B}{k_B}\right]_{\text{hyp.struct.}} = -8.71\ (3)$ ppm, where 91% of the broadening comes from the weak components around ±600 kHz.

This precise evaluation does not take into account any possible differential saturation of the absorption between strong and weak hyperfine transitions. If any, the saturation will be much more important for strong lines, which would result in higher relative intensities of the weak lines and thus an additional broadening of the whole Doppler envelope. In order to evaluate this effect, we recorded the Doppler signal and alternatively measured the relative absorption at two different laser powers (0.3 and 0.9 μW) by using optical attenuators placed either just before the photodetector or just before the absorption cell, in order to test saturation effects for a constant detected laser intensity. The absorptions were equal within 5×10^{-4}, which gives an upper limit for the saturation parameter of 3.6×10^{-3} at 1.3 Pa. This very small value is in good agreement with that expected with such laser powers, gas pressure and a typical size of the laser beam of a few mm. In the collisional regime, the saturation parameter scales as the inverse of the square

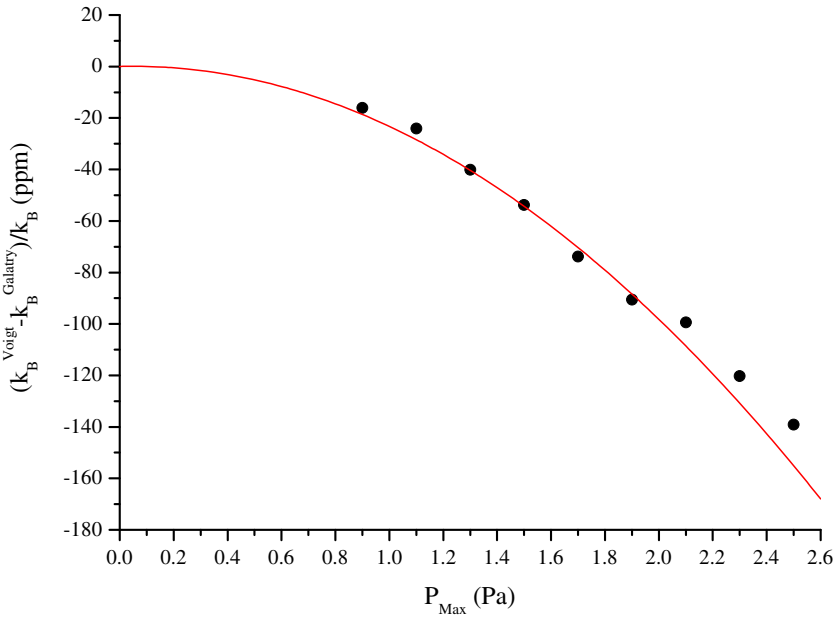

Figure 10. Relative difference in k_B determination (dots) by fitting experimental spectra with a Voigt (k_B^{Voigt}) or a Galatry ($k_B^{Galatry}$) profile when using the sub-ensemble of the spectra recorded at pressures below P_{max}. The solid line indicates the result obtained when fitting a simulated Galatry profile with a Voigt profile.

of the pressure. The associated relative broadening stays below 0.3 p.p.m. in the 0.25–2.5 Pa pressure range. Finally, it has also been checked that the choice of the individual line shape (Voigt or Galatry) does not affect the correction on k_B.

4.3.2. The collisional effects. The 7171 spectra were fitted both with a Galatry (first-order Taylor expansion) and a Voigt profile. The relative pressure broadening varies from 6.2×10^{-4} to 6.2×10^{-3} in the pressure range 0.25–2.5 Pa. A difference of 139 p.p.m. is obtained for k_B when the fits of the 7171 spectra with a Taylor expansion of either a Galatry profile or a Voigt profile are compared, and this reflects the influence of the LDM effect at high pressure (remember that high-pressure data have a stronger weight because of the better signal-to-noise ratio). This illustrates the critical role of the chosen line shape. Each point of figure 10 shows the fractional difference obtained with the sub-ensemble of these 7171 spectra recorded at pressures below a given P_{max}. Figure 10 indicates that the LDM effect is responsible for a narrowing of the Voigt profile, leading to differences in the determination of k_B equal to or larger than the current statistical uncertainty of 6.4 p.p.m. (see section 4.2.2) for pressure ranges larger than 0.5 Pa. Thus, recording spectra at pressures lower than 0.5 Pa would maintain the systematic error due to the LDM effect below 6.4 p.p.m., when using a Voigt profile. In addition, due to the quadratic dependence of this difference, we hope to rapidly reduce this effect to the level of 1 p.p.m.

Apart from the Galatry profile, various theoretical models are available in the literature, depending on the assumption made on the type of collisions between molecules [59]. The systematic effect due to the 'soft' collisions model chosen here to describe the LDM narrowing would need to be evaluated in our pressure range, by fitting data with other models that would

require precise knowledge of the specific collision kernel. In our experimental conditions (as mentioned in section 4.1.2), the pressure broadening γ_{ab} cannot be directly fitted for each individual spectrum but is obtained by adjusting a unique g, constrained to a constant value for all the spectra. Thanks to new experimental developments, we are now able to record accurate scans over 500 MHz. This will allow us in the near future to directly and accurately determine this homogeneous broadening for each individual spectrum. In particular, in this way the possible contribution of residual impurities in the absorption cell could be taken into account. This will also permit a more precise study of different line shape models. However, we expect the present study to give the right order of magnitude of the LDM narrowing contribution to the determination of k_B, whatever the chosen collisional model.

4.3.3. Other systematic effects. Attempts to observe other systematic effects due to the modulation and geometry of the laser beam were unsuccessful at the 10 p.p.m. level. We recall that it has been shown theoretically that the line shape does not depend on the laser beam geometry [53].

Taking into account both temperature inhomogeneity and stability (detailed in section 2.2) of the thermostat, no systematic effect due to the temperature control is expected on k_B at the 2.5 p.p.m. level.

Laser-power-related systematic effects due to both nonlinearity in the detection setup and saturation broadening of the molecular absorption were also investigated. It is worth noting that the saturation of the photodetector occurs above 1 mW, whereas the operating conditions are below 1 μW. The Boltzmann constant measurements were carried out at different saturation parameters (for laser power ranging from 0.5 to 1 μW at the entrance of the absorption cell). Nonlinearity in the photodetection response was evaluated by recording spectra and determining k_B at different detected powers using attenuators placed right before the photodetector, in order to work at constant molecular transition saturation. No systematic effects were observed at the 10 p.p.m. level for these two potential causes of systematic effects.

In the following table are summarized various contributions to the linewidth with their present uncertainty, which are systematic effects to be taken into account for a proper evaluation of the Doppler width. In fact, for several non-observable effects only an upper limit estimated from the signal-to-noise ratio can be given. We recall that the uncertainties must be doubled as far as the error budget of k_B is concerned (table 1).

These figures are comparing with the present statistical uncertainty of 3.2 p.p.m. on the Doppler width. Clearly, the line shape model is until now the critical point in this experiment. However, we are confident that the next-generation experiments will lead to better control of this effect, thanks to operation within a ten times lower pressure range and to a more accurate fit of individual spectra.

The value of the Boltzmann constant deduced from these 7171 points, corrected for the systematic effect due to the hyperfine structure (see section 4.3.1), is $k_B = 1.38080(20) \times 10^{-23}\,\mathrm{J\,K^{-1}}$. The combined standard uncertainty is 144 p.p.m.; this value of k_B deviates by 106 p.p.m. from that recommended by the CODATA in 2007 [15].

5. Conclusion and perspectives

We have reported recent experimental developments towards reducing the statistical uncertainty on the Boltzmann constant determined by linear absorption of ammonia around 10 μm. New

Table 1. Error budget on the determination of the linewidth in parts per million (systematic effects and relative uncertainty).

Effect	Relative contribution to the linewidth	Uncertainty
Doppler width (49.883 MHz) at 273.15 K	10^6	3.2
Collisional effects (LDM effect and homogeneous width, for the 0.25–2.5 Pa pressure range)	6.2×10^3 at 2.5 Pa	70
Hyperfine structure of the absorption line	4.355	0.015
Gas purity (partial pressure of impurities from outgassing)	<10	<10
Nonlinearity of the photodetector	<10	<10
Saturation broadening of the absorption (for the 0.25–2.5 Pa pressure range)	<10	<10
Residual optical offset (from simulations)	<1	<1
Amplitude modulation at 40 kHz (from simulations)	0.8	0.08
Differential saturation of the hyperfine components (at 0.9 μW and the 0.25–2.5 Pa pressure range)	<0.3	<0.3
Laser linewidth	<0.2	<0.2
Temperature of the gas	0	1.25
Linearity and accuracy of the laser frequency scale	0	<0.01
Transit effect (laser beam geometry)	0	0

measurements of the Doppler broadening of the ν_2 saQ(6,3) rovibrational line of ammonia close to 273.15 K led to a statistical uncertainty of 6.4 p.p.m. on k_B (after a cumulative measurement time of 70 h). The improvement in the statistical uncertainty of the Boltzmann constant measurement from 2004 onwards at the Laboratoire de Physique des Lasers and the results from other groups [31, 32, 35] are illustrated in figure 11.

This paper also presents a careful study of the influence of the hyperfine structure. Its role cannot be neglected at a few p.p.m. level, but can now be taken into account easily with negligible residual uncertainty.

The determination of k_B by laser spectroscopy is affected by several systematic effects. Some of them have been investigated, leading to a provisory conclusion that the main source of systematic effects comes from collisional effects. Their contribution to the linewidth is clearly model dependent.

At present, the most accurate value for the Boltzmann constant that can be deduced from Doppler spectroscopy at LPL is the one obtained from measurements carried out at very low pressure, below 1.3 Pa (see section 4.2.1). From the present paper, a correction due to the hyperfine structure of the probed rovibrational line needs to be applied. This correction is of $-8.71(3)$ p.p.m., leading to a refined determination of $k_B = 1.380\,704(69) \times 10^{-23}\,\mathrm{J\,K^{-1}}$. The combined standard uncertainty is dominated by two terms [42]: the statistical uncertainty of 37 p.p.m. and the collisional effects modelization systematic uncertainty of 34 p.p.m. This measurement of k_B is in agreement with the value recommended in 2007 by CODATA, $1.380\,6504(24) \times 10^{-23}\,\mathrm{J\,K^{-1}}$, within 39 p.p.m. [15].

A detailed comparison between the Voigt and the Galatry profiles convinced us that the residual error will be reduced at the p.p.m. level if the pressure in the absorption chamber

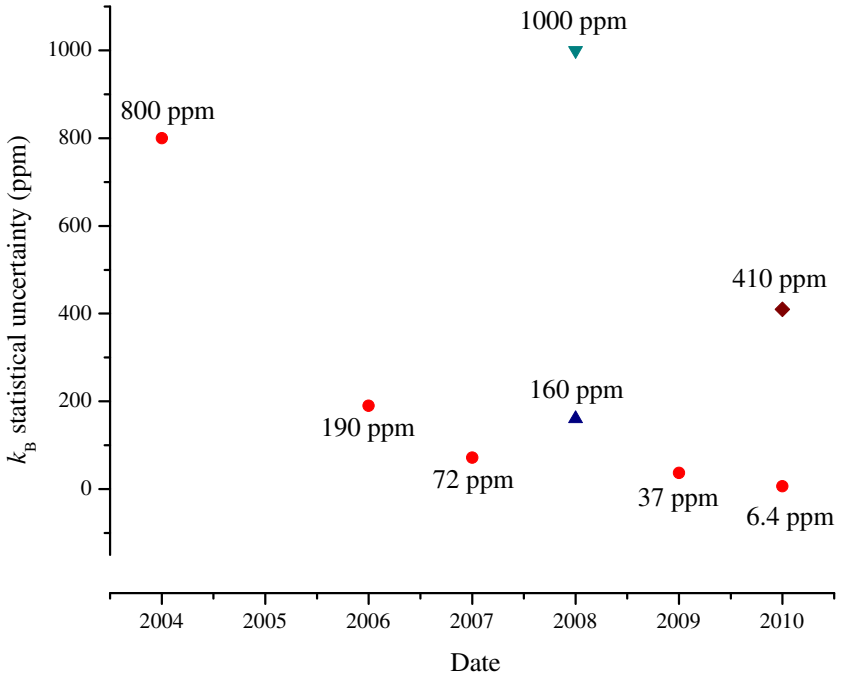

Figure 11. Statistical uncertainty on the Boltzmann constant measured by laser spectroscopy: (●) results at LPL since the first experiments in 2004 [28, 29, 40, 42, 62], (▼) results from Yamada *et al* [32], (▲) results from Casa *et al* [31] and (♦) results from Truong *et al* [35].

stays below 0.5 Pa. This major conclusion motivates the next evolution of the experimental setup. A new multi-pass Herriott cell (37 m absorption length) will be installed to record spectra at pressures ten times lower than in the experiment presented here while keeping the same signal-to-noise ratio. In this new pressure range (0.025–0.25 Pa), we expect to control the collisional effects at the p.p.m. level. In addition, a new thermostat in which the absorption cell is surrounded by a copper thermal shield located in a stainless steel enclosure was recently developed and installed. A cell temperature inhomogeneity and stability of 1 p.p.m. over one day has already been demonstrated [42]. To enable a variable working temperature, useful for a complete analysis of temperature-dependent systematic effects, the melting ice will be replaced by a 1 m^3 mixture of water and alcohol, maintained at a desired temperature. A cryostat actively coupled to a heat exchanger will permit the regulation of the liquid bath temperature from +10 °C down to −10 °C. In this temperature range, the relative uncertainty associated with the interpolated temperature measured by the SPRTs used remains within 1 p.p.m. Finally, we plan to conduct a more refined study of the possible influence of the modulation distortion connected to the nonlinearity of the photodetector.

These future developments should lead to a new value for the Boltzmann constant with an accuracy of a few p.p.m., which is the main goal of this work. It will be useful to compare this with the value obtained by the acoustic method and this hopefully will contribute significantly to the CODATA value. The determination of the Boltzmann constant by different methods with an accuracy of a few p.p.m. is a prerequisite for a new definition of the kelvin by fixing the value of k_B.

Acknowledgments

This work was funded by the Laboratoire National de Métrologie et d'Essais and the European Community (EraNet/IMERA). We thank A Amy-Klein for her critical reading of the manuscript, Y Hermier, F Sparasci and L Pitre from Laboratoire Commun de Métrologie LNE-CNAM for SPRTs calibrations, discussions and advice on the thermometry side of this study and S Briaudeau for help in designing and setting up the thermostat and temperature control devices.

References

[1] Bordé C J 2005 *Phil. Trans. R. Soc.* **363** 2177–201
[2] Wignall J W G 2007 *Metrologia* **44** 19–22
[3] Taylor B N and Mohr P J 1999 *Metrologia* **36** 63–4
[4] Fischer J *et al* 2007 *Int. J. Thermophys.* **28** 1753–65
[5] Petley B W 2007 *Metrologia* **44** 69–72
[6] Mills I M, Mohr P J, Quinn T J, Taylor B N and Williams E R 2005 *Metrologia* **42** 71–80
[7] Mills I M, Mohr P J, Quinn T J, Taylor B N and Williams E R 2006 *Metrologia* **43** 227–46
[8] Stock M and Witt T J 2006 *Metrologia* **43** 583–7
[9] Becker P 2003 *Metrologia* **40** 366–75
[10] Becker P, De Bièvre P, Fujii K, Glaeser M and Inglis B 2007 *Metrologia* **44** 1–14
[11] Cabiati F and Bich W 2009 *Metrologia* **46** 457–66
[12] Fischer J *et al* 2007 *Int. J. Thermophys.* **28** 1753–65
[13] Moldover M R, Trusler J P M, Edwards T J, Mehl J B and Davis R S 1988 *J. Res. Natl Bur. Stand.* **93** 85–144
[14] Moldover M R, Trusler J P, Edwards T J, Mehl J B and Davis R S 1988 *Phys. Rev. Lett.* **60** 249–52
[15] Mohr P J, Taylor B N and Newell D B 2008 *Rev. Mod. Phys.* **80** 633–730
[16] Pitre L, Guianvarc'h C, Sparasci F, Richard A and Truong D 2008 *Int. J. Thermophys.* **29** 1730–9
[17] Pitre L, Guianvarc'h C, Sparasci F, Guillou A, Truong D, Hermier Y and Himbert M E 2009 *C. R. Phys.* **10** 835–48
[18] Sutton G, Underwood R, Pitre L, De Podesta M and Valkiers S 2010 *Int. J. Thermophys.* **31** 1310–46
[19] De Podesta M, May E F, Mehl J B, Pitre L, Gavioso R M, Benedetto G, Giuliano Albo P A, Truong D and Flack D 2010 *Metrologia* **47** 588–604
[20] Rusby R, De Podesta M and Williams J 2005 *NPL Report* DEPC TH006
[21] Fellmuth B, Gaiser C and Fisher J 2006 *Meas. Sci. Technol.* **17** R145–59
[22] Schmidt J W, Gavioso R M, May E F and Moldover M R 2007 *Phys. Rev. Lett.* **98** 254504
[23] Fellmuth B, Fischer J, Gaiser C, Priruenrom T, Sabuga W and Ulbig P 2009 *C. R. Phys.* **10** 828–34
[24] Moldover M R 2009 *C. R. Phys.* **10** 815–27
[25] Gaiser C and Fellmuth B 2009 *Metrologia* **46** 525–33
[26] Bordé C J 2000 Conference given at *Symposium to celebrate the 125th Anniversary of the Meter Convention* (Paris: Académie des Sciences)
[27] Bordé C J 2002 *Metrologia* **39** 435–63
[28] Daussy C, Briaudeau S, Guinet M, Amy-Klein A, Hermier Y, Bordé C J and Chardonnet C 2005 *Laser Spectroscopy* ed E Hinds and E Riis (Singapore: World Scientific) pp 104–11
[29] Daussy C, Guinet M, Amy-Klein A, Djerroud K, Hermier Y, Briaudeau S, Bordé C J and Chardonnet C 2007 *Phys. Rev. Lett.* **98** 250801
[30] Daussy C, Bordé C J and Chardonnet C 2007 *Images Phys.* **2006** 80–5
[31] Casa G, Castrillo A, Galzerano G, Wehr R, Merlone A, Di Serafino D, Laporta P and Gianfrani L 2008 *Phys. Rev. Lett.* **100** 200801

[32] Yamada K M T, Onae A, Hong F-L, Inaba H, Matsumoto H, Nakajima Y, Ito F and Shimizu T 2008 *J. Mol. Spectrosc.* **249** 95–9
[33] Castrillo A, Casa G, Merlone A, Galzerano G, Laporta P and Gianfrani L 2009 *C. R. Phys.* **10** 894–906
[34] Merlone A, Moro F, Castrillo A and Gianfrani L 2010 *Int. J. Thermophys.* **31** 1360–70
[35] Truong G-W, May E F, Stace M S and Luiten A N 2011 *Phys. Rev.* A **83** 033805
[36] Wicht A, Hensley J M, Sarajlic E and Chu S 2002 *Phys. Scr.* **T102** 82–8
[37] Cladé P, De Mirandes E, Cadoret M, Guellati-Khelifa S, Schwob C, Nez F, Julien L and Biraben F 2006 *Phys. Rev. Lett.* **96** 033001
[38] Bouchendira R, Pierre Cladé P, Guellati-Khélifa S, Nez F and Biraben F 2010 arXiv:1012.3627
[39] Bradley M P, Porto J V, Rainville S, Thompson J K and Pritchard D E 1999 *Phys. Rev. Lett.* **83** 4510–3
[40] Djerroud K, Daussy C, Lopez O, Amy-Klein A, Briaudeau S, Hermier Y and Chardonnet C 2007 *Ann. Phys., Paris* **32** 175–8
[41] Bernard V, Daussy C, Nogues G, Constantin L, Durand P E, Amy-Klein A, Van Lerberghe A and Chardonnet C 1997 *IEEE J. Quantum Electron.* **QE-33** 1282–7
[42] Lemarchand C, Djerroud K, Darquié B, Lopez O, Amy-Klein A, Chardonnet C, Bordé C J, Briaudeau S and Daussy C 2010 *Int. J. Thermophys.* **31** 1347–59
[43] Gunther-Mohr G R, White R L, Schawlow A L, Good W E and Coles D K 1954 *Phys. Rev.* **94** 1184–91
[44] Gordon J P 1955 *Phys. Rev.* **99** 1253–63
[45] Hougen J T 1972 *J. Chem. Phys.* **57** 4207–17
[46] Kukolich S G and Wofsy S C 1970 *J. Chem. Phys.* **52** 5477–81
[47] Ruben D J and Kukolich S G 1974 *J. Chem. Phys.* **61** 3780–3784
[48] Ouhayoun M, Bordé C J and Bordé J 1977 *Mol. Phys.* **33** 597–600
[49] Salomon C, Chardonnet C, Van Lerberghe A, Bréant C and Bordé C J 1984 *J. Phys. Lett.* **45** L1125–9
[50] Chardonnet C, Butcher R J and Bordé C J private communication
[51] Bordé C J, Bordé J, Bréant C, Chardonnet C and Salomon C 1985 *Laser Spectrosc.* **VII** 108–13
[52] Pickett H M 1991 *J. Mol. Spectrosc.* **148** 371–7
[53] Bordé C J 2009 *C. R. Phys.* **10** 866–82
[54] Dicke R H 1953 *Phys. Rev.* **89** 472–3
[55] Galatry L 1961 *Phys. Rev.* **122** 1218–23
[56] Nelkin M and Ghatak A 1964 *Phys. Rev.* A **135** A4
[57] Rautian S G and Sobel'man I I 1967 *Sov. Phy.—Usp.* **9** 701–16
[58] Cygan A, Lisak D, Trawi'nski R S and Ciurylo R 2010 *Phys. Rev.* A **82** 032515
[59] Hartmann J-M, Boulet C and Robert D 2008 *Collisional Effects on Molecular Spectra: Laboratory Experiments and Models, Consequences for Applications* (Amsterdam: Elsevier Science)
[60] Baker C E 1969 *Nasa Technical Note* TN D-5574
[61] Pine A S, Markov V N, Buffa G and Tarrini O 1993 *Quant. Spectrosc. Radiat. Transfer* **50/4** 337–48
[62] Djerroud K, Lemarchand C, Gauguet A, Daussy C, Briaudeau S, Darquié B, Lopez O, Amy-Klein A, Chardonnet C and Bordé C J 2009 *C. R. Phys.* **10** 883–93
[63] Efron B, Tibshirani R and Tibshirani R J 1993 *An Introduction to the Bootstrap* (Boca Raton, FL: CRC Press)